Multi-objective optimization of virtual source distributions for ultrafast diverging wave imaging

Zahraa Alzein, Marco Crocco, Daniele D Caviglia, Hervé Liebgott

Ultrasonics 163 (2026) 107979

Contents lists available at ScienceDirect

Ultrasonics

journal homepage: www.elsevier.com/locate/ultras

Multi-objective optimization of virtual source distributions for ultrafast diverging wave imaging

Zahraa Alzein [a,b,*], Marco Crocco [b], Daniele D. Caviglia [a], Hervé Liebgott [c]

[a] Department of Electrical, Electronic, Telecommunications Engineering, and Naval Architecture (DITEN) University of Genoa, Genoa, 16145, Italy
[b] Esaote S.p.A, Genova, 1645, Liguria, Italy
[c] INSA-Lyon, Universite Claude Bernard Lyon 1, CNRS, Inserm, CREATIS UMR 5220, U1294, IUT Lyon 1, Lyon, 69100, France

ARTICLE INFO

Keywords:
Diverging wave
Virtual sources
Multi-objective optimization
Genetic algorithms
Spatial distribution

ABSTRACT

Diverging wave imaging (DWI) with coherent compounding addresses the field-of-view (FOV) limitations of ultrafast imaging by placing virtual sources (VSs) behind the transducer. The number and spatial distribution of these VSs affects both image quality and frame rate, making them of high interest. Existing approaches use deterministic placements (e.g., linear, tilted, and Archimedean-spiral distributions), which exhibit inherent trade-offs between resolution and contrast. However, the optimal placement of VSs to maximize image quality has not yet been investigated for convex arrays. In this study, we propose a multi-objective genetic algorithm to optimize VS spatial distributions with a compound mask weighting strategy — mapped from transmit apodization in synthetic aperture imaging (SAI) — to enhance beam coherence and reduce artifacts during optimization. The framework was evaluated across different numbers of VSs to quantify performance trade-offs under fewer transmission events. The proposed multi-objective framework optimizes two PSF-based metrics, namely the Full Width at Half Maximum (FWHM) and the Peak Sidelobe Level (PSL). Then, image-quality metrics, such as contrast ratio (CR) and signal-to-noise ratio (SNR), are computed a posteriori as independent validation measures on the reconstructed images. In both simulations and experimental trials, the optimized VS distributions achieved up to a 50% reduction in FWHM and a 60% improvement in CR compared to deterministic methods, while preserving these gains even with reduced transmission events.

1. Introduction

Ultrafast Imaging with coherent compounding has emerged as a transformative innovation in ultrasound imaging. The ability to acquire images at exceptionally high frame rates has paved the way for various applications such as shear wave elastography [1], fully quantitative Doppler flow imaging [2], and functional ultrasound imaging (fUS) [3]. Of particular importance is its role in small and micro-vessel imaging, where the rapid collection of highly resolved spatial and temporal data within a short acquisition time has greatly improved visualization and diagnostic accuracy [4,5].

Early ultrafast methods use plane waves (PWs) transmissions [6,7]. Despite their high frame rate, PWs inherently limit the FOV due to the need for sequential edge-to-edge steering, particularly in curved arrays used for abdominal or pelvic imaging [8]. To overcome FOV constraint, parallel beamforming with compounding using diverging waves (DWs) transmissions was proposed by Hasegawa and Kanai, and their method showed a comparable image quality to that of conventional methods [9]. In diverging wave imaging, the coherent compounding process is analogous to multi-elements synthetic aperture imaging, wherein signals from multiple transducer elements are coherently combined to synthesize an extended effective aperture, thereby enhancing the signal-to-noise ratio (SNR) [10].

DWs exploiting spherical wavefronts, emitted from virtual sources (VSs) placed behind the transducer, have been explored for convex array configurations. Ghigo et al. [11] investigated how the configuration of the VSs impacts image quality using a convex array. The observed performance was nearly equivalent, likely due to using only three compounding waves. An alternative method for synthesizing a wide, unfocused wavefront across the full aperture was introduced in [12,13]. This method employs a straightforward transmission strategy, a linear delay profile for convex arrays. The resulting wavefront was shown to follow an Archimedean spiral, varying with the steering angle. Another Fourier-domain beamforming approach was proposed [14], using a tilted diverging wave transmission. While this approach demonstrated enhanced image quality, its effectiveness was restricted to regions with

* Corresponding author at: Department of Electrical, Electronic, Telecommunications Engineering, and Naval Architecture (DITEN) University of Genoa, Genoa, 16145, Italy.
E-mail address: zahraa.alzein@edu.unige.it (Z. Alzein).

https://doi.org/10.1016/j.ultras.2026.107979
Received 23 July 2025; Received in revised form 21 January 2026; Accepted 25 January 2026
Available online 9 February 2026

a narrow azimuthal angle. In [15], three transmission strategies for generating diverging waves were analyzed: lateral virtual-source-based Diverging Wave Imaging (latDWI), tilted virtual-source-based Diverging Wave Imaging (tiltDWI), and Archimedean-spiral-based Imaging (AMI). latDWI achieved superior resolution compared to the other methods. However, this came at the cost of stronger axial lobe levels, leading to the poorest image contrast. In contrast, both tiltDWI and AMI offered improved image contrast, albeit with a slight reduction in resolution.

Existing studies on DWs using convex arrays have primarily focused on deterministic distributions or specific transmission strategies. While previous approaches have demonstrated improvements in resolution and contrast, they are limited by their reliance on fixed configurations. For instance, deterministic distributions, such as uniformly spaced VSs, fail to account for the spatial variations in beam coherence and sidelobe levels across the imaging field. Similarly, transmission strategies like tilted diverging waves or Archimedean spirals, while effective in specific regions, are constrained by azimuthal dependencies and may not provide uniform performance across the entire field of view. In DWs, the spatial distribution and number of VSs critically influence fundamental performance trade-offs between frame rate and image quality. As each VS corresponds to a distinct transmission event, the achievable frame rate exhibits an inverse proportionality to the number of VSs. Increasing the number of VSs enhances imaging quality by improving spatial resolution and contrast through coherent compounding of multiple diverging wavefronts, however, at the cost of framerate. Therefore, achieving a high image quality while maintaining a high frame rate of original unfocused wave imaging is of high interest.

While prior studies have explored deterministic VS distributions, this study proposes a multi-objective evolutionary optimization framework to optimize VS spatial distributions, aiming to minimize the Full Width at Half Maximum (FWHM) and Peak Sidelobe Level (PSL). The optimization framework leverages insights from prior work in related fields, where multi-objective methods have been successfully applied to solve complex trade-offs. In sparse array configurations, optimization algorithms such as simulated annealing [16] and genetic algorithms [17] have been employed to enhance lateral resolution and suppress sidelobes while minimizing the number of active elements [18]. These methods have demonstrated significant improvements in imaging quality, particularly in applications requiring high spatial resolution and low artifact levels. Similarly, in acoustic source localization [19], and radar systems [20], evolutionary optimization techniques have been used to optimize array geometries, ensuring accurate source detection even under challenging conditions, such as high noise levels or complex propagation environments.

The multi-objective genetic algorithm MOGA, from the Global Optimization Toolbox in MATLAB [21], has been chosen for optimization following better preliminary results compared to other approaches in [22]. The optimization framework was enhanced by integrating compound mask weights, which were previously derived from synthetic aperture imaging (SAI) transmit apodization. These weights were mapped to DWI using a closed-form approach, as detailed in our earlier work [23]. The compound mask adjusts the contribution of each VS to individual grid points during the optimization process. The optimization was performed using varying numbers of virtual sources (20, 10, 6, and 4) chosen to explore the trade-off between image quality and frame rate systematically and to evaluate the method's adaptability in enhancing frame rate while preserving diagnostic image quality. The optimized VSs distributions were subsequently validated using both in silico data and experimental data. The proposed multi-objective optimization framework for virtual source (VS) distribution is designed as an offline calibration procedure. The optimization algorithm is executed prior to imaging using representative simulated data to identify optimal VS spatial configurations that balance image quality and frame rate. Once these optimized configurations are obtained, they are fixed and employed during real-time ultrafast imaging acquisitions without any further computational overhead. Therefore, the approach is fully compatible with high frame rate imaging, as the computationally intensive optimization does not interfere with live data acquisition or processing.

In summary, the contributions of this work are the following:

1. We propose a multi-objective optimization framework to find the spatial distribution of virtual sources in diverging wave imaging, for improved image quality.
2. We integrate a compound mask apodization into the optimization, so that the contribution of each virtual source to each image point is weighted during optimization.
3. Through simulation and experiments We show that the optimized virtual source distributions can improve image quality compared with deterministic distributions,even with a reduced number of transmissions.

The remainder of the paper is organized as follows: Section 2 details the materials and methods, including the MOGA optimization framework, evaluation metrics, and validation setups. Section 3 presents the results, comparing optimized and deterministic VSs distributions and highlighting performance trade-offs. Section 4 concludes with key findings, their impact on ultrafast imaging, and future research directions.

2. Material and method

2.1. Multi-objective optimization framework

The genetic algorithm (GA) is a well-established optimization technique inspired by biological evolution processes [24]. In this study, GA was employed to optimize the distribution of VSs for convex arrays in DWI. The optimization process employs two fitness functions: one for the Full Width at Half Maximum (FWHM) and one for the Peak Sidelobe Level (PSL), which are critical metrics for assessing image quality in ultrasound imaging. To implement the optimization, the GA was executed in MATLAB using the `gamultiobj` function [25], and the overall framework is illustrated in Fig. 1. The following subsections detail the key components of the optimization framework, including initialization, selection, crossover, mutation, termination criteria, and post-processing steps.

2.1.1. Initialization and search space

The algorithm starts by initializing a population of 1500 individuals, with each individual $\mathbf{x}_i$ randomly sampled from a predefined search space $\mathcal{X}$. In our framework, the search space is defined by the lateral (x) and axial (z) positions of the N virtual sources (VSs) within predefined physical limits. The search space, or decision space [26], was restricted to a rectangular region to reduce the complexity of the objective functions and accelerate the optimization process [27]. The population was defined as:

$$P(0) = \{\mathbf{x}_1, \mathbf{x}_2, \ldots, \mathbf{x}_{1500}\}, \quad \mathbf{x}_i \sim \mathcal{U}(\mathcal{X}), \tag{1}$$

where $\mathcal{U}$ denotes a uniform distribution over the search space, and $\mathbf{x}_i$ represents the ith individual in the population. This random initialization promotes sufficient population diversity to support a thorough exploration of the decision space. Subsequent sections detail the fitness functions, the specific limits of the search space, and the imaging parameters adopted in this study.

2.1.2. Selection, crossover, and mutation

In multi-objective optimization, Pareto dominance is a fundamental concept where multiple conflicting objectives must be optimized simultaneously. Consider two candidate solutions, $\mathbf{x}_i$ and $\mathbf{x}_j$, each evaluated by a vector of objective functions:

$$\mathbf{f}(\mathbf{x}) = [f_1(\mathbf{x}), f_2(\mathbf{x}), \ldots, f_m(\mathbf{x})],$$

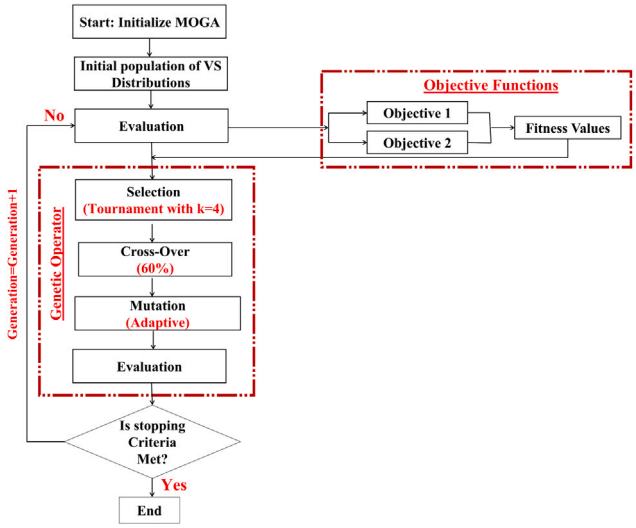

Fig. 1. Overview of the Multi-Objective Genetic Algorithm (MOGA) for optimizing virtual source (VS) distributions. The algorithm initializes a population of VSs distributions within a predefined search space and evaluates them using two objective functions. Evolutionary operations include tournament selection (k=4), crossover (60%), and adaptive mutation to refine the solutions iteratively. The process continues until convergence criteria are met, yielding an optimized set of VS configurations.

where m represents the number of objectives. A solution $\mathbf{x}_i$ is said to *dominate* another solution $\mathbf{x}_j$ (denoted $\mathbf{x}_i \prec \mathbf{x}_j$) if and only if:

$$f_k(\mathbf{x}_i) \le f_k(\mathbf{x}_j) \quad \forall k \in \{1, \dots, m\},$$
$$\text{and} \quad \exists k \quad \text{such that} \quad f_k(\mathbf{x}_i) < f_k(\mathbf{x}_j). \tag{2}$$

In other words, $\mathbf{x}_i$ is at least as good as $\mathbf{x}_j$ in all objectives and strictly better in at least one. A solution that is not dominated by any other solution in the population is called a *non-dominated solution*. The collection of all such solutions forms the *first Pareto front*, also referred to as rank 1. After removing the first Pareto front, the next set of non-dominated solutions constitutes the *second front* (rank 2), and this process continues iteratively. Solutions with a higher Pareto dominance rank are generally closer to the optimal trade-off frontier and are less dominated by other solutions.

In the context of this study, there are two objectives:

$$\mathbf{f}(\mathbf{x}) = [f_1(\mathbf{x}), f_2(\mathbf{x})], \tag{3}$$

where $f_1(\mathbf{x})$ represents FWHM and $f_2(\mathbf{x})$ represents the PSL that will be explained in detail in Section 2-B. The `gamultiobj` function automatically performs multi-objective selection based on Pareto dominance. This means that instead of ranking solutions by a single fitness score, the algorithm identifies non-dominated solutions—those that cannot be improved in one objective without degrading another. The selection process retains diverse solutions to explore trade-offs between resolution and contrast. To select individuals for reproduction, a tournament selection of size 4 was applied based on analytical studies in [28,29] that indicate tournament sizes in the range of 2–5 provide balanced selection pressure while preserving population diversity. In this process, subsets of 4 individuals were randomly selected, and the individual with the highest Pareto dominance rank within each subset was chosen as:

$$\mathbf{x}_{\text{selected}} = \arg\max_{\mathbf{x}_j} \{\mathbf{f}(\mathbf{x}_j) \mid \mathbf{x}_j \in \text{Tournament Subset}\}, \tag{4}$$

where $\mathbf{f}(\mathbf{x}_j)$ represents the multi-objective fitness evaluation of individual $\mathbf{x}_j$. For crossover, 60% of the population was combined to produce offspring based on preliminary experiments with commonly observed parameter ranges (typically 60%–90%) in genetic algorithm literature [30,31] that effectively balances exploration and exploitation for most applications. In our genetic algorithm, each individual $\mathbf{x}$ represents a candidate solution encoding the spatial coordinates of all N virtual sources:

$$\mathbf{x} = [x_1, z_1, x_2, z_2, \dots, x_N, z_N],$$

where x_n and z_n denote the lateral and axial positions of the nth virtual source, respectively. The crossover operation combines two parent individuals, $\mathbf{x}_A$ and $\mathbf{x}_B$, to generate an offspring $\mathbf{x}_{\text{child}}$ as follows:

$$\mathbf{x}_{\text{child}} = \alpha \mathbf{x}_A + (1 - \alpha)\mathbf{x}_B, \quad \alpha \in [0, 1], \tag{5}$$

where α is a random weighting factor that introduces variability while preserving key traits from the parent solutions. The offspring inherit beneficial characteristics from both parents, promoting convergence toward optimal solutions. Then, a mutation was applied to the individuals. The mutation operation for a*gene* x_j within a chromosome $\mathbf{x}$ that corresponds to a single coordinate value (either lateral or axial) of one virtual source. The mutation operation perturbs this gene by adding a small random offset δ:

$$x_j^{\text{mutated}} = x_j + \delta, \quad \delta \sim \mathcal{U}([-\Delta, \Delta]), \tag{6}$$

where $\mathcal{U}([-\Delta, \Delta])$ denotes a uniform distribution over the interval $[-\Delta, \Delta]$. It represents the feasible mutation range dynamically adjusted during optimization by `mutationadaptfeasible` function, which modifies the size of the mutation step based on the boundaries of the variables and the current search space to ensure that the algorithm explores the search space effectively without premature convergence.

2.1.3. Termination criteria and non-dominated solutions (NDSs)

The algorithm terminated under the following criteria:

- A maximum of 500 generations was reached.
- No significant improvement in the NDSs was observed over 50 consecutive generations, with a tolerance of 5%.

The chosen criteria balanced computational efficiency and thorough exploration of the search space, ensuring that the algorithm converged to high-quality solutions without excessive computational overhead. Fitness evaluation was performed for each individual to compute the objectives of FWHM and PSL, defined in the next subsection. The optimization sought non-dominated solutions, representing trade-offs between FWHM and PSL. To formally define dominance, a solution $\mathbf{x}_i$ is considered non-dominated if there exists no other solution $\mathbf{x}_j$ in the population such that

$$f_k(\mathbf{x}_i) \le f_k(\mathbf{x}_j) \quad \forall k, \quad \text{and} \quad \exists k \text{such that} f_k(\mathbf{x}_i) < f_k(\mathbf{x}_j),$$

where f_k denotes the kth objective function. Here, $\mathbf{x}_i$ and $\mathbf{x}_j$ represent two distinct candidate solutions, each encoding the spatial coordinates of virtual sources. The resulting Non-dominated solutions provide valuable insights into the trade-offs between resolution and contrast, enabling the selection of optimal VS configurations for specific imaging scenarios.

The main genetic algorithm (GA) settings used in this study are summarized in Table 1. These parameters were kept fixed for all VS configurations (20, 10, 6, and 4 VSs).

2.1.4. Parallel computing and clustering

To accelerate the evaluation process, MATLAB's Parallel Computing Toolbox [32] was used, significantly reducing runtime by enabling parallel fitness calculations. Once the non-dominated solutions (NDSs) were identified,k-means clustering was applied using MATLAB's Statistics and Machine Learning Toolbox [33] based on similarity in objective space to reduce redundancy among the final NDSs solutions.

Table 1
Genetic algorithm (GA) parameters used for VS optimization. All parameters were kept fixed across the different VS configurations (20, 10, 6, and 4 VSs).

Parameter	Value
Optimizer	`gamultiobj` (MOGA)
Population size	1500 individuals
Selection scheme	Tournament (k = 4)
Crossover fraction	0.60
Mutation operator	`mutationadaptfeasible`
Max. generations	500
Stall generations	50
Stall tolerance	5%
Initial population	Uniform in $\mathcal{X}$

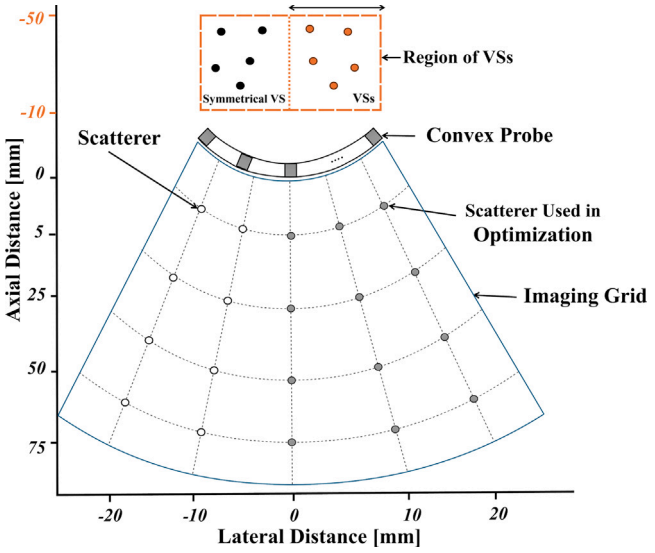

Fig. 2. Study configuration from top to bottom: the arrangement of VSs, where the orange VSs indicate those selected for optimization; a convex probe with N elements; scatterer positions, with gray ones used in the optimization process; and the imaging grid defining the region of interest.

2.2. Evaluation metrics

The imaging performance of the virtual source (VS) distributions was quantitatively assessed using two key metrics: *Full Width at Half Maximum (FWHM)* and *Peak Sidelobe Level (PSL)*. These metrics are widely recognized in ultrasound imaging for evaluating lateral resolution and contrast, respectively, and were employed to ensure a comprehensive assessment of image quality across the imaging volume. The FWHM quantifies the lateral resolution of the imaging system by measuring the width of the main lobe of the Point Spread Function (PSF) at −6 dB relative to its peak intensity [34]. The PSL measures the contrast degradation caused by sidelobes [35], which is critical to distinguish low-contrast structures such as cysts or lesions. The PSL was computed as the ratio of the amplitude of the highest sidelobe to the amplitude of the main lobe, expressed in decibels (dB). The sidelobe peaks were identified using a peak detection function, `findpeaks`[36], ensuring precise localization of the highest sidelobe.

In the optimization process, to evaluate the imaging performance across the field of view, FWHM and PSL values were computed for a set of scatterers located at different depths and lateral positions within the imaging volume to ensure a robust assessment of imaging quality across the entire volume, capturing variations in resolution and contrast at different spatial locations. The values of FWHM and PSL were concatenated into two datasets, denoted as $\mathcal{D}_{\text{FWHM}}$ and $\mathcal{D}_{\text{PSL}}$, respectively:

$$\mathcal{D}_{\text{FWHM}} = [\text{FWHM}_1, \text{FWHM}_2, \ldots, \text{FWHM}_N](mm) \tag{7}$$

$$\mathcal{D}_{\text{PSL}} = [\text{PSL}_1, \text{PSL}_2, \ldots, \text{PSL}_N](dB) \tag{8}$$

where N represents the total number of scatterers used for evaluation. The optimization process aimed to minimize two objective functions derived from the FWHM and PSL datasets. The first objective function, $f_1(\mathbf{x})$, was defined as the mean value of the FWHM data set, $\mathcal{D}_{\text{FWHM}}$, which represents the average lateral resolution across the image volume. The second objective function, $f_2(\mathbf{x})$, was defined as the mean value of the PSL dataset, $\mathcal{D}_{\text{PSL}}$, representing the average sidelobe level. These objectives were formulated as:

$$f_1(\mathbf{x}) = \text{avg}(\mathcal{D}_{\text{FWHM}}), \tag{9}$$

$$f_2(\mathbf{x}) = \text{avg}(\mathcal{D}_{\text{PSL}}), \tag{10}$$

where avg$(\cdot)$ denotes the arithmetic mean. By minimizing Objective$_1$, the optimization process sought to enhance lateral resolution, while minimizing Objective$_2$ aimed to reduce sidelobe levels, thereby improving contrast and reducing image artifacts. The use of average values for the objective functions prioritizes consistent imaging performance across the field of view, avoiding biases that could arise from extreme values in the datasets. It is important to emphasize that FWHM and PSL are the only two quantities included in the multi-objective fitness vector of the genetic algorithm and thus constitute the actual optimization objectives. Other image-quality metrics used in this study, such as the contrast ratio (CR) computed on anechoic cysts and the SNR estimated,are evaluated on the beamformed images as independent validation measures.

2.3. Simulation setup

The received raw data were generated using the Field II software [37,38], using a 128-element convex array transducer with a center frequency of $f_0 = 3$ MHz, pitch 0.4246 mm, and radius 41.2 mm, reproducing the geometry of the CA5-2 probe used in the experiments. The transducer was excited with a 2-cycle sinusoidal signal and with a sampling frequency of 12 MHz. A Hanning window was applied for both transmit (TX) and receive (RX) apodization, with the window scaled according to the aperture size in receive, the latter being set according to the focal number equal to 0.7. Compound mask weights, defined as functions of the virtual source (VS) positions, were mapped directly from synthetic aperture imaging transmit apodization [23] to ensure that only contributions from properly insonified regions were retained. Subsequently, the simulated RF signals were processed using a standard time-domain delay-and-sum beamforming algorithm. Beamforming was carried out on a polar (r, θ) imaging grid consistent with the convex geometry of the transducer. The beamforming process was followed by coherent recombination of data related to each VS position, weighted by the above defined compound mask, envelope extraction, and logarithmic compression to produce B-mode images.

For the optimization step, the setup included 20 point scatterers distributed at various depths of $[5, 25, 50, 75]$ mm along the lateral positions of the axial direction $[-20, -10, 0, 10, 20]$ mm. All scatterers were assigned equal amplitudes to ensure uniform reflectivity. This discrete grid of point reflectors was used solely to evaluate the image-quality metrics (FWHM and PSL) for each candidate VS distribution in the multi-objective optimization. Fig. 2 illustrates the organization of the imaging grid and the distribution of the virtual sources (VS) utilized in the multi-objective optimization process. The lateral positions (x) of the VSs were constrained between 0 mm and 27.2 mm, corresponding to half the total lateral width of the convex array. Axial positions (z) were restricted to a range between −50 mm and −10 mm. These constraints ensured that each VS remained within the practical imaging boundaries.

To reduce computational complexity, symmetry about the transducer's central axis was exploited: only half of the total number of

VSs was explicitly optimized, and the remaining VSs were mirrored. Consequently, configurations with 20, 10, 6, and 4 VSs were optimized by considering only 10, 5, 3, and 2 VSs, respectively. This approach effectively halves the dimensionality of the decision space; rather than optimizing $2N$ parameters (the x and z positions for N VSs), only N are considered. Similarly, the symmetry reduces the number of scatterers needed, from an initial set of 20 scatterers, only 12 were required for the optimization since symmetrical scatterer positions yield identical image-quality metrics. This symmetry constraint is a methodological trade-off: by enforcing symmetry of the VS positions around the transducer center, the dimensionality of the search space and the computational cost are substantially reduced.

2.4. Deterministic distributions

For direct comparison with the optimized genetic algorithm solutions, two deterministic configurations of 20 virtual sources (VSs) were evaluated: a linear arrangement and a curvilinear arrangement selected based on configurations investigated in prior studies [15], serving as established references for comparison. In both cases, all VSs were positioned at the same axial distance of $R_{\text{convex}} = 50$ mm from the probe surface. In the linear arrangement, the 20 VSs were uniformly spaced across a lateral range spanning -32 to $+32$ times the transducer pitch (pitch = 425.56 μm). For the curvilinear arrangement, the VSs follows a curvilinear pattern that aligns with the geometry of the probe, with angular placement of the sources confined within a maximum aperture angle of 33°, distributed symmetrically about the central axis of the probe. Figs. 6(a) and 6(b) shows the spatial distribution of linear and curvilinear VS distributions, respectively. In this work, these two families (linear and curvilinear VS distributions placed along a circular arc behind the probe) are used as deterministic baselines for convex-array DWI. They are consistent with standard implementations of diverging-wave imaging for 2D convex probes and provide simple, interpretable reference configurations for assessing the impact of the proposed optimization. More elaborate deterministic or semi-optimized layouts (e.g., spiral or tilted trajectories) typically introduce additional design parameters and are often investigated in the context of 3D or matrix–array imaging.

2.5. Phantom with anechoic cysts and reflectors

To evaluate the imaging performance of the optimized virtual source (VS) distributions, a synthetic phantom was designed to simulate a tissue-mimicking environment for 2D ultrasound imaging. The phantom dimensions were defined to match the convex transducer footprint, with its lateral extent determined by the number of elements and their respective pitch. The axial depth extended to 70 mm, starting from 5 mm below the transducer surface. Within this domain, scatterers were randomly distributed with lateral and axial positions sampled from a uniform distribution. Their amplitudes followed a Gaussian distribution to mimic the heterogeneous nature of biological tissues. The synthetic phantom includes anechoic cysts and high-amplitude reflectors to assess contrast and spatial resolution. Specifically, 9 anechoic cysts — scatterer-free regions — were positioned at axial depths of 20 mm, 40 mm, and 60 mm. The cysts of radii of 2 mm, 3 mm, and 4 mm, respectively, with lateral positions spanning from −20 mm to 20 mm. The regions ensure the creation of distinct low-echo zones, enabling a quantitative assessment of contrast on envelope images. The contrast ratio (CR) was computed as:

$$CR = 20\log_{10}\left(\frac{\mu_{\text{in}}}{\mu_{\text{out}}}\right), \tag{11}$$

where μ_{in} and μ_{out} denote the mean pixel intensities inside and outside the cyst region, respectively. The high-amplitude point reflectors were placed at axial depths of 10 mm, 30 mm, and 50 mm, with lateral positions ranging from -20 mm to 20 mm. Their amplitude was scaled by a factor of 10 relative to the background scatterers, ensuring strong reflectivity. All deterministic and optimized VS distributions obtained through the multi-objective optimization framework were used to reconstruct B-mode images of the synthetic phantom. The simulation process was conducted under the same imaging configuration described previously in Section 2.3.

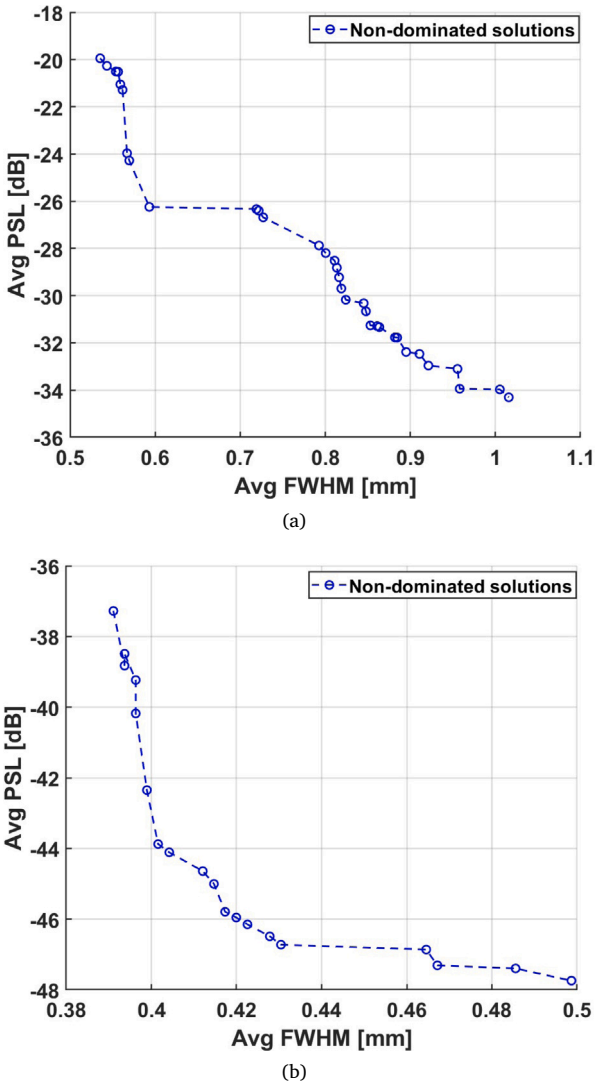

Fig. 3. Impact of the compound mask on the optimization of Virtual Source (VS) distributions using a Genetic Algorithm (GA):(a) Pareto front showing the average values of Full Width at Half Maximum (FWHM) and Peak Sidelobe Level (PSL) obtained from GA optimization without the compound mask.(b) Pareto front obtained from GA optimization with the compound mask.

2.6. Experiments

To further test the robustness of the optimized VS experimental trials were conducted using a Vantage 256 ultrasound research scanner (Verasonics, Redmond, WA, USA) and CA5-2 curved array with 128 elements ($Radius$ = 41.2 mm, $pitch$ = 424.56 μm, f_0 = 3 MHz). The excitation parameters are set the same as in Section 2-C. The sampling rate was set to 12 MHz, and imaging was performed on the 410SCG LE Multi-Purpose Accreditation Phantom. The acquired RF data were subsequently beamformed and processed to evaluate imaging performance metrics contrast, and resolution. The full aperture is used for transmission.

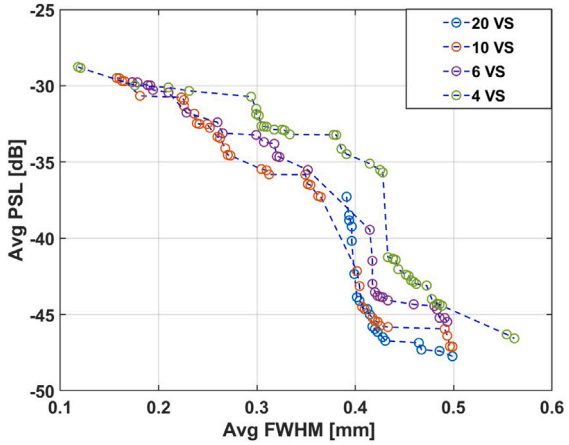

Fig. 4. Pareto-optimal front for different numbers of Virtual Sources (VSs) in the optimization process: 20 VSs (blue), 10 VSs (orange), 6 VSs (purple), and 4 VSs (green).

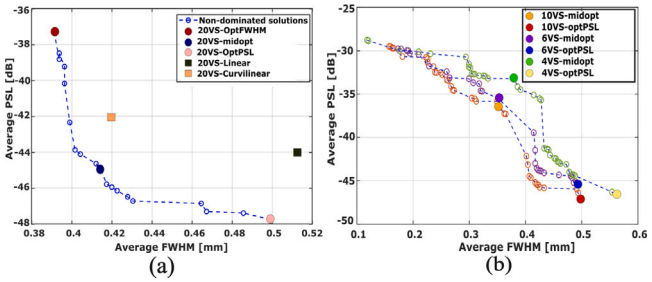

Fig. 5. The Pareto front for 20 VSs (a) includes three selected solutions: **optFWHM** (red), **midopt** (dark blue), and **optPSL** (light pink) alongside deterministic configurations: **20VS-linear** (green square) and **20VS-curvilinear** (orange square).(b) represents the Pareto fronts for reduced VS configurations (10, 6, and 4 VSs) feature two selected solutions — **midopt** and **optPSL** — for each case. The selected solutions for 10 VSs (orange and red), 6 VSs (purple and blue), and 4 VSs (green and yellow) respectively.

2.7. Compound mask weights

The compound mask weights were introduced in our earlier study in [23], where, under the assumption of a short-duration transmit pulse, the linear relation between synthetic aperture imaging(SAI) apodization and DWI compound weights is approximated by a diagonal matrix, yielding a mapping based on a straightforward geometric rule. For both linear and convex arrays, this mapping is accomplished by interpolating the apodization profile at the intersection point between the probe surface and the line connecting a VS with an imaging point, so that any apodization profile used in SAI can be adequately transformed to DWI compound weights as a function of virtual source positions. Therefore, applying transmit apodization in DWI ultrafast imaging as a function of virtual sources, which improves image quality with a negligible computational cost, and these weights are integrated into the multi-objective optimization algorithm to enhance both image quality metrics. The physical impact of the compound mask on beam coherence and sidelobe suppression has been investigated in detail in our previous work [23,39,40]. There, representative point-spread functions, sidelobe envelopes, and contrast metrics were compared for DWI with and without the compound mask, for both linear and convex probes, showing that the mask effectively redistributes energy from sidelobes toward the main lobe, leading to narrower effective PSFs and improved cyst contrast with negligible computational overhead. In the present study, we therefore use the compound mask formulation as a fixed and previously validated weighting scheme, and focus the optimization on the spatial distribution of virtual sources.

3. Results

3.1. Optimization results with and without compound mask

The set of non-dominated solutions (NDSs) commonly referred to as the Pareto-optimal front [41,42], resulting from the optimization of virtual source (VS) distributions, with and without the application of a compound mask, are illustrated in Fig. 3(a) and Fig. 3(b), respectively using 20 VSs. These plots demonstrate the trade-offs between average FWHM and average PSL, where a decrease in average PSL generally accompanies an increase in average FWHM, and vice versa. The set of (NDSs) obtained using the compound mask consistently outperforms those without the mask across both metrics. The Pareto fronts of NDSs, exhibit discontinuities. Such discontinuities are commonly observed in multi-objective optimization problems and arise due to the inherent structure of the non-dominated solution set (NDS) [43]. The use of the compound mask significantly enhanced imaging quality, as reflected in the improved trade-offs between FWHM and PSL. Without the compound mask, the average FWHM ranged from 0.6 mm to 1.0 mm, while the average PSL spanned −18 dB to -34 dB. In contrast, applying the compound mask improved values of 0.38 mm to 0.5 mm for FWHM and −36 dB to −48 dB for PSL, corresponding to improvements of 37% and 41%, respectively. These enhancements are attributed to the weighting mechanism introduced by the compound mask, which prioritizes contributions from regions exhibiting higher beam coherence while effectively suppressing sidelobe artifacts. Unlike conventional coherent compounding methods, which fail to adapt to varying insonification conditions, the compound mask adjusts the transmission weights for each virtual source position, addressing the limitations of traditional approaches, particularly in convex arrays, where the insonification field is inherently non-uniform.

3.2. Optimization results with different number of virtual sources

Fig. 4 presents the optimal Pareto fronts obtained for configurations with 20, 10, 6, and 4 VSs, illustrating the trade-off between the Avg FWHM and the Avg PSL. The Pareto fronts in Fig. 4 exhibit visible gaps and discontinuities along some regions of the curves. This behavior is expected and reflects the intrinsic structure of the optimization problem rather than numerical instability or insufficient sampling. In particular, the joint FWHM–PSL objective landscape is highly non-convex and multi-modal over a bounded VS search space, and the Pareto set is sampled with a finite population size. As a result, some regions of the objective space contain few or no feasible solutions with significantly different FWHM/PSL trade-offs, which appears as gaps along the estimated front. These discontinuities therefore interpreted as a consequence of the underlying problem geometry and discrete sampling, not as artifacts of the genetic algorithm. As expected, the configuration with 20 VSs offers the most favorable balance between resolution and contrast, achieving Avg FWHM values between 0.38 mm and 0.55 mm and Avg PSL levels approaching −50 dB. However, reducing the number of VSs does not severely compromise image quality, thanks to the robustness of the proposed optimization framework. For instance, with 10 VSs, the Pareto front shifts to achieve an Avg FWHM below 0.2 mm, while Avg PSL degrades by roughly 3–5 dB relative to the 20-VS configuration. A similar trend is observed with 6 VSs, where the Avg FWHM remains in the range of less than 0.45 mm and the Avg PSL hovers around −45 dB. Even with just 4 VSs, the method continues to preserve image quality, maintaining Avg FWHM values typically below 0.6 mm and Avg PSL near −45 dB.

3.3. Selection of representative pareto-optimal solutions

To assess the impact of different optimized VS configurations on imaging performance, three specific solutions were selected from the

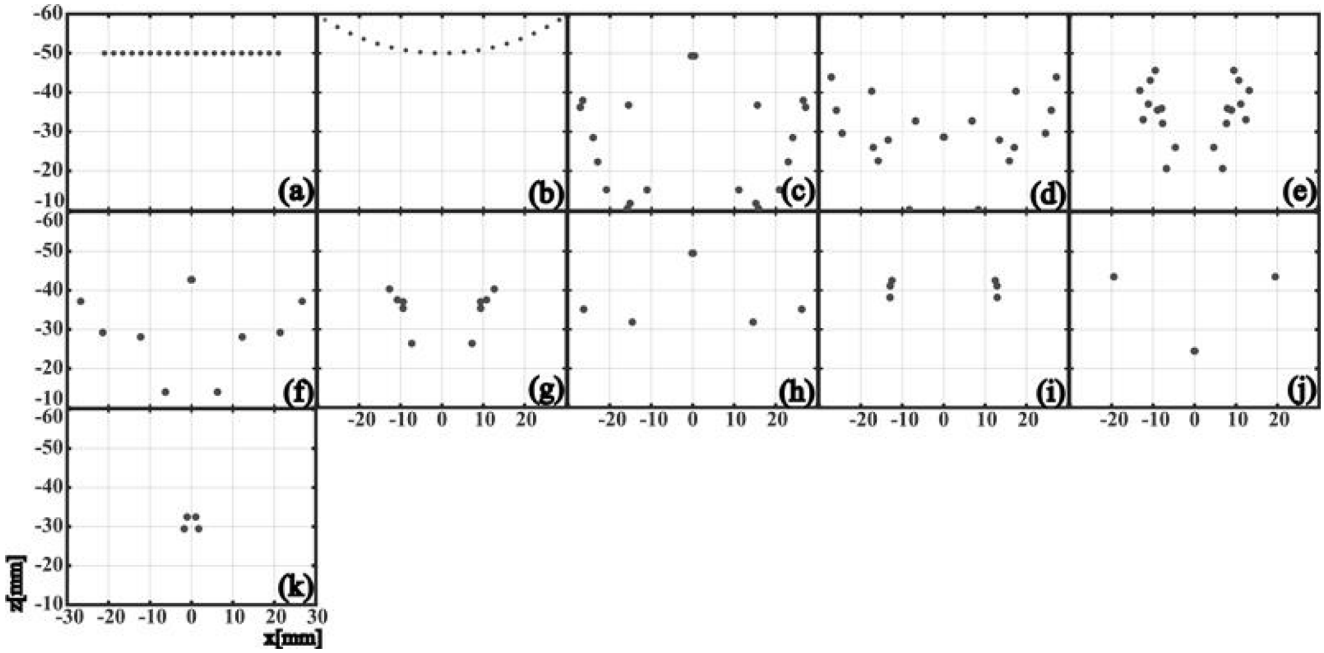

Fig. 6. Spatial distribution of VSs for both deterministic and optimized distributions chosen for validation:(a) 20VS-Lin, (b) 20VS-Curv, (c) 20VS-optFWHM, (d) 20VS-midopt, (e) 20VS-optPSL, (f) 10VS-midopt, (g) 10VS-optPSL, (h) 6VS-midopt, (i) 6VS-optPSL, (j) 4VS-midopt, (k) 4VS-optPSL.

Pareto-front for further validation:

- **Optimized for FWHM(optFWHM)**: Prioritizing minimum beamwidth, offering higher lateral resolution at the expense of increased PSL.
- **Optimized for PSL(optPSL)**: Prioritizing lower sidelobe levels, improving contrast while allowing for a slightly broader main lobe.
- **Mid-range trade-off(midopt)**: A balanced solution, offering an intermediate compromise between resolution and contrast. In this region, several neighboring Pareto-optimal points exhibit very similar FWHM/PSL values, so selecting any of these nearby solutions would lead to essentially the same image-quality metrics. The midopt configuration is therefore used as an illustrative compromise operating point within this cluster, rather than as a unique recommended optimum.

Fig. 5 illustrates the chosen solutions based on visual inspection of the objective space and corresponding image quality metrics from the Pareto front for the 20 VS configuration, plotted alongside deterministic VS distributions (linear and curvilinear) previously described in Section 2-D (Fig. 5(a)). For lower VS configurations (10, 6, and 4 VSs) (Fig. 5(b)), the selection strategy was adapted based on the trade-offs observed in the Pareto front. The optimized FWHM solutions for these configurations exhibited significantly higher PSL levels, which would lead to degraded image quality. Therefore, only solutions corresponding to the mid-range trade-off and optimized PSL were selected for validation. These choices ensure that the imaging performance remains comparable to the 20 VS configuration. The spatial distributions of the selected VS configurations across all tested cases (20, 10, 6, and 4 VSs) are visualized alongside the deterministic ones in Fig. 6. The solutions chosen for the midoptFWHM configuration in Fig. 6 — panels (d), (f), (h), and (j) corresponding to 20, 10, 6, and 4 VS transmissions, respectively — illustrate spatial distributions where one of the VS is placed along the central axis. As a result, its symmetry VS will be aligned with it. This central alignment was previously demonstrated in [44], which showed that positioning one VS at the center is advantageous. However, in our study, such centering was not necessarily in optimizing PSL levels, as evidenced by the optimized configurations in Fig. 6 panels (e), (g), (i), and (k), where the sources are distributed asymmetrically around the axis. All the selected solutions were evaluated through both simulation-based and experimental validation and analyzed quantitatively using metrics such as *FWHM*, and *contrast ratio (CR)* to validate performance.

3.4. Simulation results

The reconstructed B-mode images for the synthetic phantom, described in Section 2-E, are presented in Fig. 7. These images illustrate the performance of both optimized chosen solutions and deterministic VSs configurations. The FWHM was measured on high-intensity reflectors, while the CR was computed for anechoic cysts, as defined by Eq. (10). The quantitative results are summarized using boxplots in Fig. 8, showing the values of FWHM(a) and CR(b) across different imaging regions. The optimized solution for FWHM (**optFWHM**) with 20 VSs achieved a median FWHM of 0.5 mm, a 50% reduction compared to curvilinear and linear deterministic distributions (1.0 mm and 1.1 mm, respectively). Similar performance was observed for mid-optimal (**midopt**) solutions with fewer VSs: 10 VSs achieved a median FWHM of 0.55 mm (45%–50% reduction), while 6 VSs and 4 VSs maintained FWHM values of 0.6 mm and 0.65 mm, respectively. The optimized configurations with fewer VSs outperform deterministic configurations with 20 VSs. Although only FWHM and PSL enter the multi-objective optimization as cost functions, CR is computed on the resulting images as an validation metric to assess how the changes in PSF-based objectives translate into cyst contrast. The optimized solution for PSL (**optPSL**) with 20 VSs achieved a median CR of −16 dB, a 25%–30% improvement over deterministic curvilinear and linear distributions (−12 dB and −10 dB, respectively) Similar trends were observed for reduced (**optPSL**) VS configurations: 10 VSs maintained a CR of −15 dB, while 6 VSs and 4 VSs achieved −15.5 dB and −14 dB, respectively. Optimized solutions consistently outperformed deterministic distributions, even with fewer transmission events.

3.4.1. SNR for deterministic and optimized distributions

In addition to FWHM and CR, we quantified the impact of the different virtual source (VS) distributions on the image signal-to-noise ratio

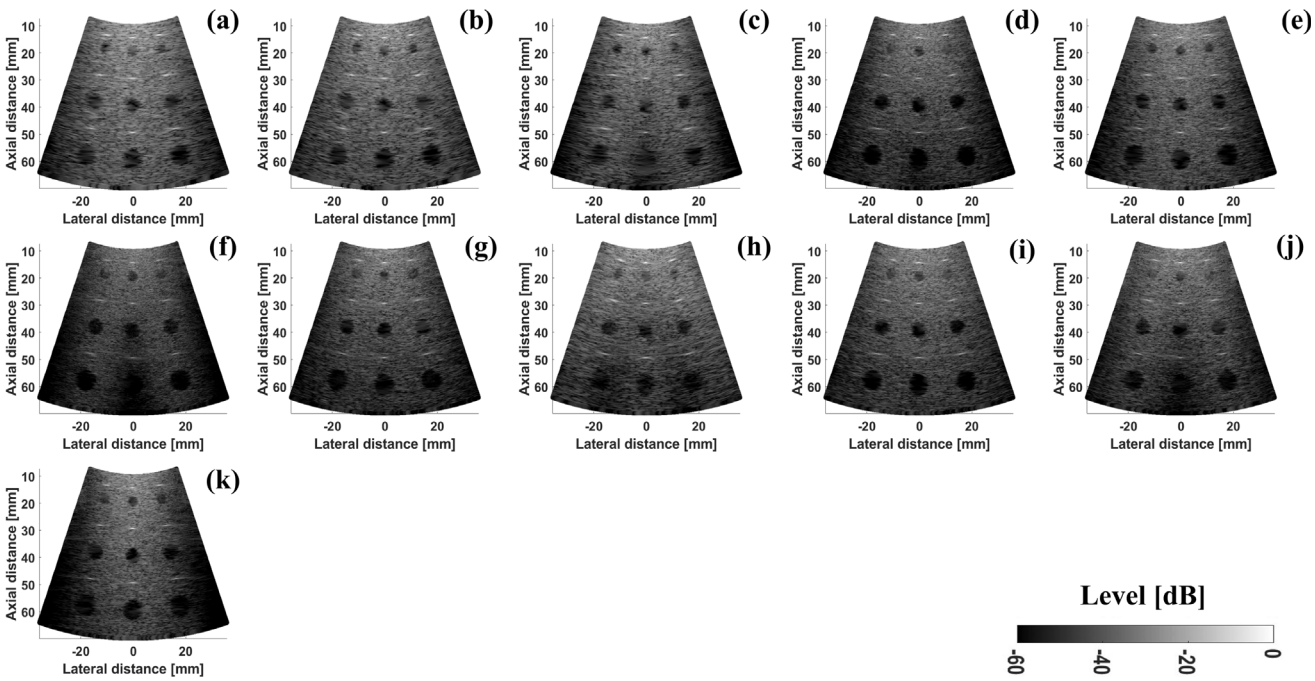

Fig. 7. B-mode images of the simulated phantom with anechoic cysts and reflectors for(a) 20VS-Lin, (b) 20VS-Curv, (c) 20VS-optFWHM, (d) 20VS-midopt, (e) 20VS-optPSL, (f) 10VS-midopt, (g) 10VS-optPSL, (h) 6VS-midopt, (i) 6VS-optPSL, (j) 4VS-midopt, and (k) 4VS-optPSL.

(SNR) using the simulated data. For each VS configuration (deterministic and optimized), RF data were first generated in Field II as described in Section 2.3. To emulate electronic noise in a physically realistic way, zero-mean Gaussian noise was added at the receive-channel level before RX beamforming for each transmit event. Specifically, for transmit index k and receive channel c, the noisy RF signal was modeled as

$$r_{k,c}(t) = s_{k,c}(t) + n_{k,c}(t), \tag{12}$$

where $s_{k,c}(t)$ denotes the noiseless Field II RF signal and $n_{k,c}(t)$ is a zero-mean white Gaussian noise process, $n_{k,c}(t) \sim \mathcal{N}(0, \sigma_{\text{ch}}^2)$, independent across channels and transmissions. The variance σ_{ch}^2 controls the absolute noise level and was chosen to obtain a moderate SNR regime comparable to typical experimental conditions; the *relative* SNR differences between the various VS distributions were found to be robust to the specific value of σ_{ch}^2.

To separate signal and noise contributions, we generated two beamformed datasets for each VS configuration. First, the noiseless RF data $s_{k,c}(t)$ were beamformed and coherently compounded over all VSs using the standard delay-and-sum pipeline, yielding a complex noiseless beamformed signal $a_{\text{sig}}(x, z)$ at each image point (x, z). Second, the noisy RF data $r_{k,c}(t)$ were processed with the same beamformer, producing a complex noisy beamformed signal $a_{\text{sig+noise}}(x, z)$. A complex noise-only beamformed image was then obtained by subtraction in the complex domain, before envelope extraction,

$$a_{\text{noise}}(x, z) = a_{\text{sig+noise}}(x, z) - a_{\text{sig}}(x, z). \tag{13}$$

The corresponding envelope images were computed as

$$I_{\text{sig}}(x, z) = \left|a_{\text{sig}}(x, z)\right|, \qquad I_{\text{noise}}(x, z) = \left|a_{\text{noise}}(x, z)\right|, \tag{14}$$

where $I_{\text{sig}}(x, z)$ represents the signal-only envelope image and $I_{\text{noise}}(x, z)$ represents the noise-only envelope image. All subsequent SNR calculations were performed on these envelope images in linear scale; log-compression was used only for visualization of B-mode images.

To estimate SNR, we selected a homogeneous background region-of-interest (ROI), Ω_{b}, located in speckle-only tissue, outside the anechoic cysts and away from the high-amplitude point reflectors. In practice, Ω_{b} was chosen as a rectangular ROI at intermediate depths (e.g., between 40 mm and 50 mm) and within a central lateral range (e.g., between −10 mm and 10 mm). Let $I_{\text{sig}}(x, z)$ and $I_{\text{noise}}(x, z)$ for $(x, z) \in \Omega_{\text{b}}$ denote the signal-only and noise-only envelope values inside this ROI. The mean signal amplitude in the ROI was computed as

$$\mu_{\text{sig}} = \frac{1}{|\Omega_{\text{b}}|} \sum_{(x,z)\in\Omega_{\text{b}}} I_{\text{sig}}(x, z), \tag{15}$$

and the noise standard deviation was computed from the noise-only image as

$$\sigma_{\text{noise}} = \sqrt{\frac{1}{|\Omega_{\text{b}}| - 1} \sum_{(x,z)\in\Omega_{\text{b}}} I_{\text{noise}}^2(x, z)}, \tag{16}$$

where $|\Omega_{\text{b}}|$ denotes the number of pixels in the ROI. The image SNR for a given VS distribution was then defined as

$$\text{SNR} = \frac{\mu_{\text{sig}}}{\sigma_{\text{noise}}}, \tag{17}$$

and expressed in decibels as

$$\text{SNR}_{\text{dB}} = 20 \log_{10}\left(\frac{\mu_{\text{sig}}}{\sigma_{\text{noise}}}\right). \tag{18}$$

The above procedure was applied identically to simulated configurations (linear and curved deterministic VS distributions, as well as the different optimized VS layouts), allowing a direct comparison of the SNR achieved by each transmit strategy. The corresponding results are presented in Table 2. The optimized VS distributions led to a clear increase in SNR compared with the deterministic layouts. For the 20 VS configurations, the SNR improved from $\text{SNR}_{\text{dB}} = 16.0$ dB (20VS-Lin) and 16.8 dB (20VS-curv) to 18.2 dB (20VS-optFWHM), 18.8 dB (20VS-midopt), and 19.4 dB (20VS-optPSL), i.e., an SNR gain of approximately 2–3.5 dB.

Even when reducing the number of transmissions, the optimized layouts still provide higher SNR than the deterministic references; for example, 10VS-midopt achieves 17.8 dB, which remains above the 20VS-Lin configuration.

3.5. Experimental results

The optimized sequences presenting the most outperforming ones in comparison with the deterministics (linear and curvilinear) are

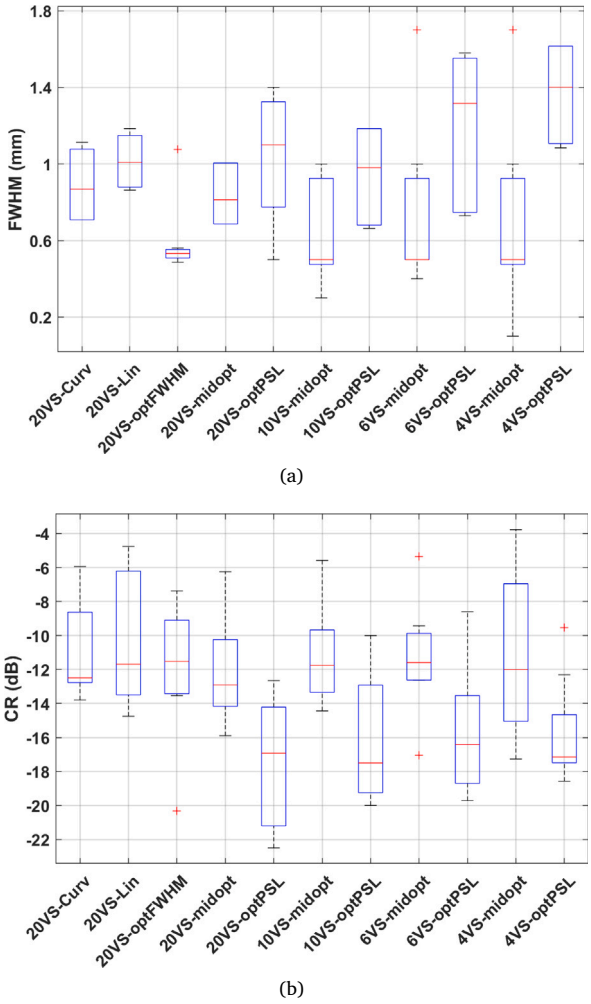

Fig. 8. Boxplots for (a) FWHM measured on the 9 reflectors (b) CR measured on 9 anechoic cysts from the phantom images(Fig. 7) for all selected VSs.

Table 2
SNR values for different virtual source (VS) distributions. SNR is computed in a homogeneous background ROI (depth 40–50 mm, lateral −10 to 10 mm).

VS distribution	SNR (linear)	SNR (dB)
20VS-Lin	6.31	16.0
20VS-curv	6.90	16.8
20VS-optFWHM	8.10	18.2
20VS-midopt	8.70	18.8
20VS-optPSL	9.30	19.4
10VS-midopt	7.80	17.8
4VS-midopt	6.50	16.3

then implemented on a Vantage 256 ultrasound research scanner. The B-mode images of the tissue-mimicking phantom obtained with the deterministic distribution are shown in Fig. 9, and with 20 VS optimized in Fig. 10, and with a reduced number of VSs in Fig. 11, illustrating the performance of both deterministic and chosen optimized(VSs) distributions.

The FWHM was measured on the point scatterers, and the CR ratio was measured on the anechoic cyst located at 45 mm. The numerical results for FWHM and CR are summarized in a box plot in Fig. 12 and Table 3, respectively. The **optFWHM** solution with 20 VSs achieved a median FWHM of 0.9 mm, representing reductions of 35.7% and 28.6% from the linear (**20VS-Lin**, 1.4 mm) and curvilinear (**20VS-Curv**, 1.26 mm) configurations, respectively. The mid-optimal solution

Table 3
CR values measured on anechoic cyst located at 45mm from the phantom images (Fig. 9, 10 and 11) for selected VSs.

Virtual source distribution	CR [dB]
20VS-Lin	−16.66
20VS-Curv	−8.1027
20VS-optFWHM	−15.21
20VS-midopt	−27
20VS-optPSL	−26
10VS-midopt	−20.3
4VS-midopt	−17.35

(**20VS-midopt**) maintained a median FWHM of 1.0 mm, corresponding to reductions of 28.6% and 20.6%. Similar trends were observed with fewer VSs: the **10VS-midopt** achieved an FWHM of approximately 0.6 mm (≈ 52%), while the 4 VS midopt solutions demonstrated approximately FWHM values of 0.8 mm (36% reduction) and 0.7 mm (44% improvement over **20VS-Curv**), respectively. CR measurements (Table 3) indicate enhanced contrast performance for optimized distributions. The **optPSL** solution with 20 VSs achieved a CR of −26 dB, a 60% improvement over the curvilinear deterministic distribution (−8.1 dB). The mid-optimal solution (**20VS-midopt**) reached −27 dB, a 62.5% improvement. For reduced VS configurations, the **optPSL** solution with 10 VSs achieved −20.3 dB (40% improvement), while 4 VS configurations yielded CR values of −17.9 dB (32.4% improvement), respectively. The experimental results confirm that the proposed method demonstrates robust performance on the Verasonics Vantage 256 scanner, closely aligning with the trends observed in the simulations.

4. Discussion

In this study, a multi-objective optimization approach was introduced with compound mask weights mapped from transmit apodization in SAI to jointly optimize two PSF-based image-quality metrics in DWI, namely lateral resolution (quantified by FWHM) and sidelobe-related contrast (quantified by PSL). Metrics such as the contrast ratio (CR) on anechoic cysts and the SNR in a homogeneous background were then evaluated as independent validation measures. . The approach optimizes the spatial distributions of VSs through genetic algorithms for the simulation setup described in II-E, using convex array geometry. In-silico data and in-vitro data evaluations in Section 2 demonstrated that optimized solutions can produce improved image quality that is incomparable to deterministic distributions (i.e., linear, curvilinear). The proposed algorithm was able to produce high-quality images even with few transmission events (6 VSs, 4 VSs) with an approximately fourfold acceleration factor. Considering that optimized VSs with 6 and 4 transmissions can achieve comparable and even better image quality than 20 VSs distributed in a deterministic way, as shown in Fig. 9, the frame rate can be increased from 550 fps to 1833 and 2750 fps, respectively, for a depth of 70 mm. The ability to maintain the tradeoff between avgFWHM (resolution) and avgPSL (contrast) with fewer VSs (e.g., 4–6 VSs) challenges the conventional assumption that more transmission events are necessary for high-quality imaging. This suggests that the spatial arrangement of VSs rather than their sheer number, plays an equivalent role in optimizing beam coherence and sidelobe suppression. The compound mask's weights, which have not been introduced before for unfocalized transmissions using DWs further enhance this effect by prioritizing contributions from regions with higher coherence, as observed in Fig. 3. For example, optimized distributions with 6 VSs achieved a median FWHM of 0.6 mm and a CR of −15.5 dB, outperforming deterministic distributions with 20 VSs (Fig. 8), effectively eliminating redundant VSs while preserving essential spatial sampling.

The optimization framework is specifically tailored for convex array transducers, which limits its generalizability to other transducer

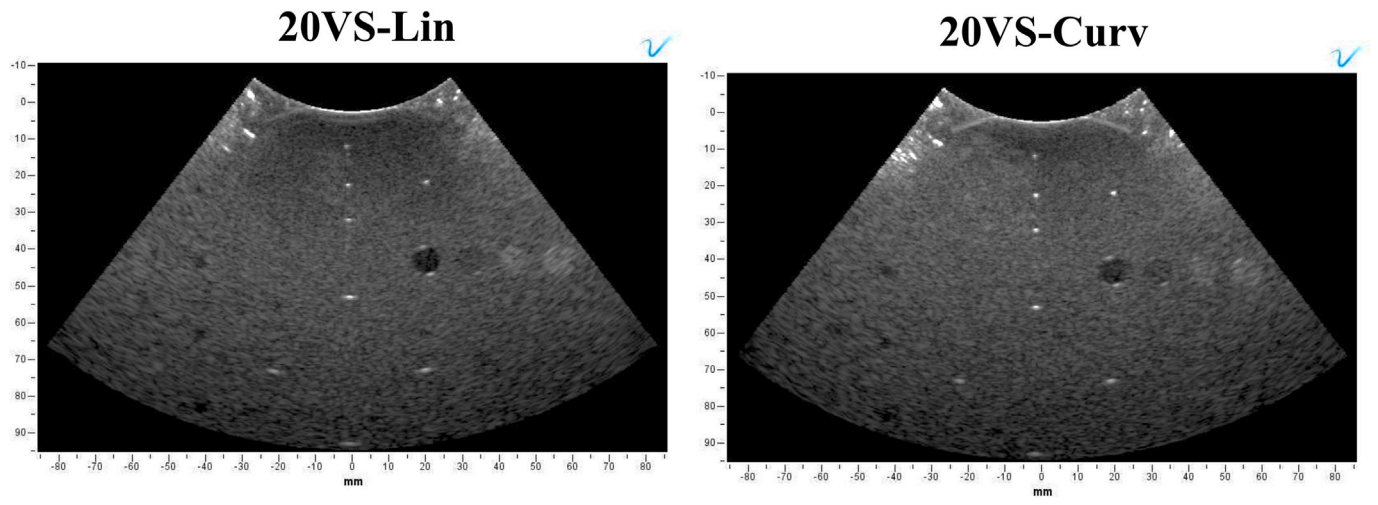

Fig. 9. B-mode images of the multi-purpose phantom acquired from the Verasonic scanner for left: 20VS-Lin,right:20VS-Curv.

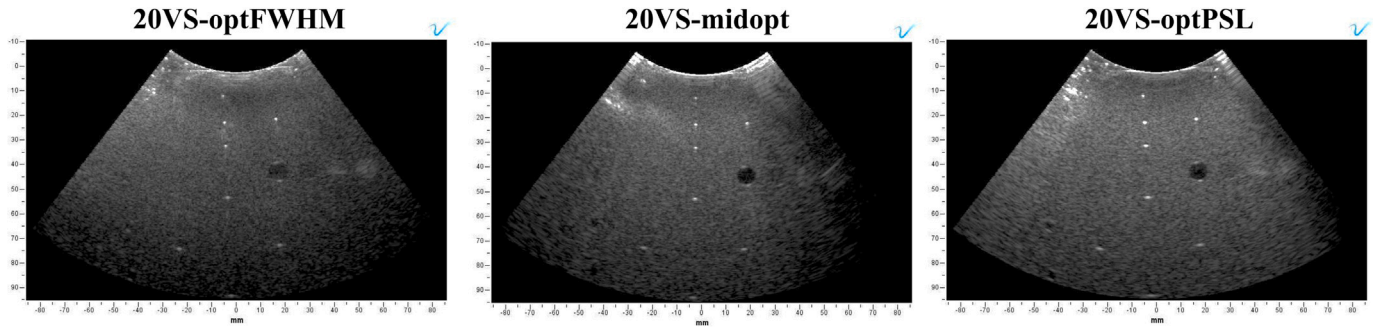

Fig. 10. B-mode images of the multi-purpose phantom acquired from the Verasonic scanner for 20VS-optFWHM, 20VS-midopt, 20VS-optPSL.

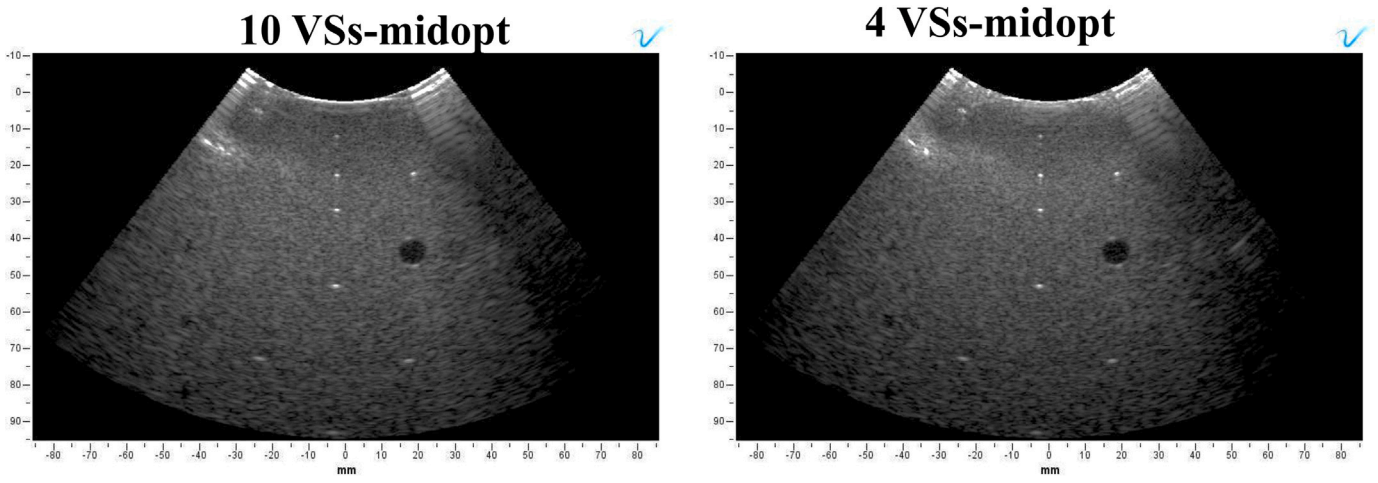

Fig. 11. B-mode images of the multi-purpose phantom acquired from the Verasonic scanner for 10VS-midopt, 4VS-midopt.

geometries, such as linear or phased arrays. The simulations conducted in this study also assume ideal acoustic conditions, neglecting the presence of noise and other real-world imaging artifacts. A limitation of the present study is the imposed symmetry of the VS distributions with respect to the array center. While this choice is well suited to the symmetric phantoms and imaging geometry considered here and greatly reduces the computational burden, it does not rule out the possibility that asymmetric VS configurations could be advantageous in heterogeneous or anatomically asymmetric scenarios. Extending the proposed optimization framework to without the symmetry constraint, possibly in combination with region-of-interest targeting, is an interesting direction for future work but of high computational demand. In clinical settings, factors such as thermal noise, electronic noise, and acoustic clutter can degrade image quality, particularly in regions with low signal-to-noise ratio (SNR). The absence of noise in the simulations may overestimate the performance of the optimized VS distributions, especially in deep tissue imaging where signal attenuation is significant. Noise models in the simulation framework could be added to

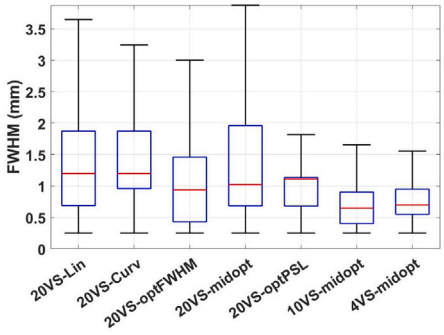

Fig. 12. Boxplots for FWHM measured on the 6 reflectors from the phantom images (Fig. 9,10, and 11) for selected VSs.

evaluate the robustness of the optimized distributions under realistic SNR conditions. Techniques such as coded excitation [45] could be employed to enhance SNR and mitigate the impact of noise, ensuring that the optimized VS distributions maintain their performance in clinical environments. The fitness functions used in the optimization process focus primarily on resolution (FWHM) and contrast (PSL), without explicitly considering the homogeneity of the PSF across the imaging volume. While the compound mask weighting strategy ensures coherent contributions from individual VS, it does not guarantee uniform PSF characteristics throughout the field of view (FOV). Additional metrics into the fitness functions could be added, such as the standard deviation of PSF intensity or spatial uniformity of sidelobe levels, to ensure more consistent imaging performance across the entire volume.

The ability to acquire high-quality images at high frame rates using the proposed multiobjective optimization framework is essential for a wide range of clinical applications, particularly in shear wave elastography and Doppler flow imaging, where real-time monitoring of dynamic physiological processes is critical. In Doppler imaging, a usable Doppler signal requires repetition of the same transmission sequence to form an ensemble. When different VSs are used, the number of distinct DW transmissions in that sequence must remain limited, because the whole sequence has to be repeated very rapidly to preserve temporal resolution and frame rate. One possible strategy is to transmit once with a small set of VSs, coherently compound them, and then repeat this short sequence to build the Doppler ensemble; alternatively, a sliding-window approach over a larger set of VSs could be envisaged. In both cases, the optimized VS distributions proposed in this work are expected to be beneficial because they improve the beam pattern and thus the spatial resolution of the compounded images. Compared with conventional focused strategies, which require N repeated transmissions on each scan line (and then the same N repetitions on the next line, and so on), DW imaging insonify the entire region with each transmission. This provides a continuous series of temporal samples for all image lines simultaneously, improving spectral resolution and enabling more precise clutter filtering from a given acquisition time. While the validation is restricted to controlled simulation and in-vitro phantom experiments where these scenarios are well suited to isolate the effects of VS optimization on resolution, sidelobes, contrast, and SNR, they do not fully capture the complexity of in vivo imaging (e.g., motion, heterogeneous attenuation, physiological clutter). Confirming the clinical relevance of the optimized VS distributions will require dedicated in vivo studies in specific diagnostic settings. The framework also provides a solid foundation for extending the optimization of virtual source (VS) distributions to 3D imaging, where the concept of the compound mask has not yet been introduced. In 3D imaging, the spatial distribution of VSs becomes even more critical due to the increased complexity of volumetric beamforming and the need for uniform coverage across a larger imaging volume. The computational time is acceptable for an offline 2D calibration step with up to 20 VSs on a standard workstation, the cost would increase substantially for larger VS sets or for 3D matrix–array configurations, from a computational standpoint, the main bottleneck of the proposed framework is the repeated PSF simulation and beamforming required to evaluate the multi-objective fitness functions within the GA. In the present 2D convex-array setting, the resulting offline computation time remains manageable, but extending the approach to significantly larger VS sets or to full 3D matrix–array imaging would markedly increase the runtime and memory requirements. In such scenarios, practical adoption would likely require more efficient implementations, such as GPU-accelerated beamforming, parallel evaluation of candidate solutions, or reduced-order parametric models of the VS distributions. We also emphasize that the optimization is intended as an offline calibration step, run once per probe and sequence configuration, so that the real-time imaging chain is not affected by the optimization cost, even though scalability remains an important consideration for future 3D applications.

5. Conclusion

This study introduced a multiobjective optimization framework for optimizing virtual source (VS) distributions in Diverging Wave Imaging (DWI), in which the genetic algorithm explicitly minimizes FWHM and PSL as the two optimization objectives, achieving significant improvements in image quality. The optimized configurations demonstrated up to a **50% reduction in FWHM** and a **60% improvement in CR**, outperforming deterministic distributions. The gains were preserved even with fewer VSs, enabling high-frame-rate imaging while maintaining diagnostic quality. Experimental validation using a Verasonics Vantage 256 scanner confirmed the framework's effectiveness, with optimized solutions consistently achieving superior resolution and contrast. The findings underscore the potential of the proposed method to enhance clinical ultrasound imaging, particularly in applications requiring real-time monitoring and high frame rates. Future work will explore extending this framework to 3D imaging scenarios.

CRediT authorship contribution statement

Zahraa Alzein: Writing – original draft, Validation, Software, Methodology, Investigation, Data curation, Conceptualization. **Marco Crocco:** Supervision, Review. **Daniele D. Caviglia:** Supervision, Funding acquisition. **Hervé Liebgott:** Supervision, Methodology, Conceptualization, Review.

Declaration of competing interest

The authors declare the following financial interests/personal relationships which may be considered as potential competing interests: Daniele D. Caviglia reports financial support was provided by University of Genoa.

Acknowledgment

This material is based on work done at the ISO 9001:2015 Pilot facility. This work was performed within the framework of the LABEX PRIMES (ANR-11-LABX-0063) of Université de Lyon.

Data availability

Data will be made available on request.

References

[1] J. Bercoff, et al., Supersonic shear imaging: A new technique for soft tissue elasticity mapping, IEEE Trans. Ultrason. Ferroelectr. Freq. Control 51 (4) (2004) 396–409.

[2] J. Bercoff, et al., Ultrafast compound Doppler imaging: Providing full blood flow characterization, IEEE Trans. Ultrason. Ferroelectr. Freq. Control 58 (1) (2011) 134–147.

[3] E. Mace, et al., Functional ultrasound imaging of the brain: Theory and basic principles, IEEE Trans. Ultrason. Ferroelectr. Freq. Control 60 (3) (2013) 492–506.

[4] P. Song, et al., Ultrasound small vessel imaging with block-wise adaptive local clutter filtering, IEEE Trans. Med. Imaging 36 (1) (2017) 251–262.

[5] D. Maresca, et al., Noninvasive imaging of the coronary vasculature using ultrafast ultrasound, J. Amer. Coll. Cardiol. Imag. 11 (6) (2018) 798–808.

[6] L. Sandrin, S. Catheline, M. Tanter, X. Hennequin, M. Fink, Time-resolved pulsed elastography with ultrafast ultrasonic imaging, Ultrason. Imag. 21 (4) (1999) 259–272.

[7] M. Tanter, M. Fink, Ultrafast imaging in biomedical ultrasound, IEEE Trans. Ultrason. Ferroelectr. Freq. Control. 61 (1) (2014) 102–119, http://dx.doi.org/10.1109/TUFFC.2014.2882.

[8] T.L. Szabo, P.A. Lewin, Ultrasound transducer selection in clinical imaging practice, J. Ultrasound Med. 32 (4) (2013) 573–582.

[9] H. Hasegawa, H. Kanai, High-frame-rate echocardiography using diverging transmit beams and parallel receive beamforming, J. Med. Ultrason. 38 (3) (2011) 129–140.

[10] K.L. Gammelmark, J.A. Jensen, Multielement synthetic transmit aperture imaging using temporal encoding, IEEE Trans. Med. Imaging 22 (4) (2003) 552–563.

[11] N. Ghigo, A. Ramalli, S. Ricci, P. Tortoli, H. Liebgott, Sequence optimization for high frame rate imaging with a convex array, in: Proc. IEEE Int. Ultrason. Symp., IUS, Las Vegas, NV, USA, 2020, pp. 1–4, http://dx.doi.org/10.1109/IUS46767.2020.9251286.

[12] A. Besson, F. Wintzenrieth, B. Hériard-Dubreuil, C. Cohen-Bacrie, On archimedean-spiral-based imaging, in: Proc. IEEE Int. Ultrason. Symp., IUS, Las Vegas, NV, USA, 2020, pp. 1–4, http://dx.doi.org/10.1109/IUS46767.2020.9251833.

[13] A. Besson, F. Wintzenrieth, C. Cohen-Bacrie, Vector-flow imaging in convex-array configurations, in: Proc. IEEE Int. Ultrason. Symp., IUS, Las Vegas, NV, USA, 2020, pp. 1–4, http://dx.doi.org/10.1109/IUS46767.2020.9251541.

[14] S. Liang, L. Wang, Fourier beamformation for convex-array diverging wave imaging using virtual sources, IEEE Trans. Ultrason. Ferroelectr. Freq. Control 69 (5) (2022) 1625–1637, http://dx.doi.org/10.1109/TUFFC.2022.3158930.

[15] S. Liang, L. Wang, A study of wide unfocused wavefront for convex-array ultrasound imaging, Ultrasonics 134 (2023) http://dx.doi.org/10.1016/j.ultras.2023.107080.

[16] S. Kirkpatrick, C.D. Gelatt, M.P. Vecchi, Optimization by simulated annealing, Science 220 (4598) (1983) 671–680.

[17] J.H. Holland, Adaptation in Natural and Artificial Systems: An Introductory Analysis with Applications to Biology, Control, and Artificial Intelligence, Univ. Michigan Press, Oxford, England, 1975.

[18] E. Roux, A. Ramalli, P. Tortoli, C. Cachard, M.C. Robini, H. Liebgott, 2-D ultrasound sparse arrays multidepth radiation optimization using simulated annealing and spiral-array inspired energy functions, IEEE Trans. Ultrason. Ferroelectr. Freq. Control 63 (12) (2016) 2138–2149.

[19] F. Le Courtois, J.-H. Thomas, F. Poisson, J.-C. Pascal, Genetic optimization of a plane array geometry for beamforming. Application to source localization in a high-speed train, J. Sound Vib. 371 (2016) 78–93.

[20] R.L. Haupt, Thinned arrays using genetic algorithms, IEEE Trans. Antennas and Propagation 42 (7) (1994) 993–999.

[21] Global Optimization Toolbox, MathWorks, Natick, MA, USA, 2021.

[22] G. Le Moign, P. Masson, O. Basset, H. Liebgott, Optimized virtual sources distributions for 3-D ultrafast diverging wave compounding imaging: A simulation study, IEEE Trans. Ultrason. Ferroelectr. Freq. Control 70 (10) (2023) 1319–1328.

[23] Z. Alzein, M. Crocco, D.D. Caviglia, Compound mask for divergent wave imaging in medical ultrasound, IEEE Access 13 (2025) 59675–59686, http://dx.doi.org/10.1109/ACCESS.2025.3557085.

[24] Z. Michalewicz, M. Schoenauer, Evolutionary algorithms for constrained parameter optimization problems, Evol. Comput. 4 (1) (1996) 1–32.

[25] Global Optimization Toolbox, MathWorks, Natick, MA, USA, 2021.

[26] C.A. Coello, G.B. Lamont, D.A. Van Veldhuizen, Evolutionary Algorithms for Solving Multi-Objective Problems, second ed., Springer, Cham, Switzerland, 2007.

[27] M.C. Robini, Theoretically grounded acceleration techniques for simulated annealing, in: I. Zelinka, V. Snášsel, A. Abraham (Eds.), Handbook of Optimization, vol. 38, Springer, Berlin, Germany, 2013, pp. 311–335.

[28] D.E. Goldberg, K. Deb, A comparative analysis of selection schemes used in genetic algorithms, in: Foundations of Genetic Algorithms, University of Illinois at Urbana-Champaign, 1991.

[29] A. Brindle, Genetic algorithms for function optimization, (Ph.D. dissertation), Dept. of Computer Science, University of Alberta, 1981.

[30] A.E. Eiben, J.E. Smith, Introduction to Evolutionary Computing, second ed., Springer, 2003.

[31] D. Whitley, A genetic algorithm tutorial, Stat. Comput. 4 (2) (1994) 65–85.

[32] Parallel Computing Toolbox, Version 7.6, The MathWorks, Inc., Natick, MA, USA, 2024.

[33] MATLAB, Version R2024a, MathWorks, Natick, MA, USA, 2024, [Online]. Available: https://www.mathworks.com.

[34] H. Liebgott, F. Cervenansky A. Rodriguez-Molares, J.A. Jensen, O. Bernard, Plane-wave imaging challenge in medical ultrasound, in: Proc. IEEE Int. Ultrason. Symp., IUS, 2016, pp. 1–4.

[35] T.L. Szabo, Diagnostic Ultrasound Imaging: Inside Out, Academic, New York, NY, USA, 2004.

[36] MATLAB, Signal Processing Toolbox User's Guide, The MathWorks, Inc., Natick, MA, USA, 2024, [Online]. Available https://www.mathworks.com/help/signal/ref/findpeaks.html.

[37] J.A. Jensen, N.B. Svendsen, Calculation of pressure fields from arbitrarily shaped, apodized, and excited ultrasound transducers, IEEE Trans. Ultrason. Ferroelectr. Freq. Control 39 (2) (1992) 262–267.

[38] J.A. Jensen, Field: A program for simulating ultrasound systems, Med. Biol. Eng. Comput. 34 (1) (1996) 351–352.

[39] Z. Alzein, H. Liebgott, M. Crocco, D.D. Caviglia, Experimental validation of compound mask for enhanced diverging wave ultrasound imaging, in: IEEE International Ultrasonics Symposium, IUS, Utrecht, Netherlands, 2025, pp. 1–3, http://dx.doi.org/10.1109/IUS62464.2025.11201552.

[40] Z. Alzein, H. Liebgott, M. Crocco, D.D. Caviglia, Virtual source-based apodization for diverging wave imaging: An experimental study, Ultrasonic Imaging http://dx.doi.org/10.1177/01617346251411346.

[41] C.A. C. Coello, G.T. Pulido, M.S. Lechuga, Handling multiple objectives with particle swarm optimization, IEEE Trans. Evol. Comput. 8 (3) (2004) 256–279.

[42] K. Deb, S. Agrawal, A. Pratap, T. Meyarivan, A fast elitist non-dominated sorting genetic algorithm for multi-objective optimization: NSGA-II, in: Parallel Problem Solving from Nature PPSN VI, vol. 1917.

[43] K. Deb, Multi-Objective Optimization Using Evolutionary Algorithms, Springer, London, U.K., 2001, p. 25, [Online]. Available https://link.springer.com/chapter/10.1007/978-0-85729-652-8_1.

[44] C. Papadacci, M. Pernot, M. Couade, M. Fink, M. Tanter, High contrast ultrafast imaging of the heart, IEEE Trans. Ultrason. Ferroelectr. Freq. Control. 61 (2) (2014) 288–301.

[45] F. Zhao, L. Tong, Q. He, J. Luo, Coded excitation for diverging wave cardiac imaging: a feasibility study, Phys. Med. Biol. 62 (4) (2017) 1565–1584, http://dx.doi.org/10.1088/1361-6560/aa58d7.